ELSEVIER

Journal of Membrane Science 120 (1996) 169–185

journal of MEMBRANE SCIENCE

Are pore size distributions in microfiltration membranes measurable by two-phase flow porosimetry?

Leos Zeman [1]

39 Hammond Place, Woburn, MA 01801, USA

Received 13 February 1996; revised 11 April 1996; accepted 11 April 1996

Abstract

The issue of evaluating equivalent pore diameter distributions in membrane microfilters from gas–liquid (g–l) porosimetry data has been critically examined. Experiments performed with one isotropic and one composite anisotropic membrane in both possible orientations revealed conspicous dependence of the obtained (g–l) porosimetry peaks on imposed pressure ramp rates, ρ. Interference of this kinetic effect can be eliminated from the measured data by extrapolation to $\rho = 0$. The ramp rate effect is most likely caused by tortuous pore length distribution, and relatively long times required for liquid expulsion. For two experiments, the observed effects of ρ could be reconciled with predictions of the Schlesinger–Bechhold theory [Bechold et al., Kolloid Z., 55 (1931) 172–198]. The data obtained with the thin top layer of the composite membrane facing intruding air directly did deviate somewhat from the theory. Pores characterized by (g–l) porosimetry are likely of the "throat type", and their size distribution is considerably more narrow than that obtained for the "node-type" pores by SEM-image analysis [Zeman and Denault, J. Membrane Sci., 71 (1992) 221–231]. A single bivariate distribution function was constructed for these two distinct pore populations. Flow-weighted or number fraction distributions can be calculated from the extrapolated porosimetry data. For narrow ranges of "throat" diameters, these distributions are fairly similar.

Keywords: Membrane preparation and structure; Microfiltration; Microporous and porous membranes; Two-phase porosimetry; Ultrafiltration

1. Introduction

Over the last thirty years, synthetic polymeric and, to a lesser extent, sintered inorganic membranes capable of stream component separations in the microfiltration (MF) and ultrafiltration (UF) size range have gained considerable technological and economic importance. Since the pioneering work of Bechhold in Germany in 1906 [1], the challenge of a reliable determination of pore size distributions in these membrane filters has been a subject of fruitful research for most of the century. Even Einstein published a short paper on the subject of experimental determination of microfilter pore size in 1923 [2]. The vast subject of MF/UF membrane characterization was recently critically reviewed by the author [3]. Over the years, much ingenuity has been employed by numerous scientists and engineers to develop reliable techniques for determining the often elusive pore size distributions in fine filtration mem-

[1] Consulting Scientist.

PII S0376-7388(96)00120-2

branes. Most of the techniques are based on one of the three following principles: (a) pore meniscus phenomena describable by the de Laplace–Young equation for the mechanical equilibrium [4] and the related Kelvin equation for the thermodynamic equilibrium; (b) fractionation of polydisperse solutes or particles describable (under proper conditions) by laws of steric retention such as the Ferry equation [5]; (c) electron microscopic visualization of surface-contained pores coupled to quantitative image analysis [6,7]. The published attempts to use gas permeability measurements (the Poiseuille–Knudsen method) [8–10] yielded only mean hydraulic radii. Measurements of gas diffusion rates through liquid-filled membranes [11,12] have been useful for detecting defects in membranes or assembled membrane devices. The underlying physical principles of most characterization techniques are relatively simple, and well understood. The main difficulties stem from the fact that most technologically important MF/UF membranes possess complex pore structures of a disordered and stochastic character. Frequently, the membranes are endowed with some degree of structural anisotropy or discontinuity. In many cases, it is next to impossible to define adequately the location, boundaries, shape, and surface character of the function-controlling "pores". Different techniques are sensitive to different subclasses of the membrane pore space, and yield, therefore, substantively different results. Description of an irregular and poorly defined pore by a single number (radius, diameter, hydraulic radius, mean flow radius, mean intercept length, equivalent radius, etc.) is deceivingly simplistic. Yet, the concept of a pore size distribution is firmly rooted in the membrane literature and practice. It will not be quite possible to avoid it in the analysis and discussion presented below. In many "real-life" MF/UF membranes, the pore space can be roughly subdivided into nodes (voids, cages, cells) that account for most of the pore volume, and throats (apertures, necks) that control permeability and sieving [3]. Dimensions of throats are typically smaller than those of nodes. The use of a bivariate pore size distribution function has been suggested for such structures [13]. It requires combined application of two different characterization techniques (e.g. some kind of intrusion porosimetry combined with thermoporometry (for ultrafilters) or microscopic image analysis). The use of a bivariate distribution function is illustrated in this report.

The methods of two-phase (flow) porosimetry are of great practical importance. They are relatively rapid and inexpensive (especially in their automated and computer-controlled versions), reasonably precise, reproducible, and non-destructive. Consequently, they represent methods of choice for quality control of MF and UF membrane products in industrial practice. Gas–liquid (g–l) porosimetry has been accepted in several versions as the ASTM standard methodology (ASTM F-316-86, ASTM E-1294-89) for pore size characterization of MF membranes.

Selection of the two immiscible fluids (Phases A

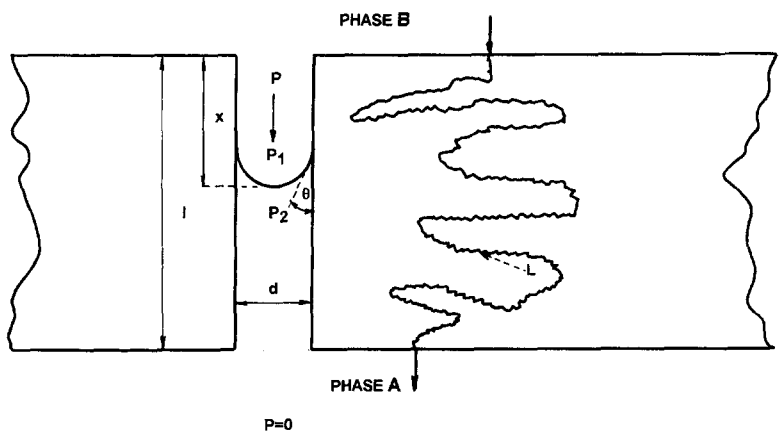

Fig. 1. Schematic drawing showing intrusion of two membrane pores by air (phase B). Left, a straight cylindrical pore; right, a tortuous maze pore. All symbols are defined in the Discussion.

and B in Fig. 1) is governed by the value of interfacial tension, γ, that is required for performing porosimetry experiments at reasonably low transmembrane pressures, usually below 100 psi (690 kPa). Liquid–liquid (l–l) porosimetry which employs a pair of immiscible liquids with values of γ in the range of 0–3 dyn/cm (e.g. *n*-butanol–water; $\gamma = 1.7$ dyn/cm) is suited for the mesopore ($d = 2$ to 50 nm) range typical for UF membranes. The concepts presented here apply also to ultrafilters and the important (l–l) porosimetry technique. However, the work is primarily focused on MF membranes and their characterization by (g–l) porosimetry. In typical (g–l) experiments, membrane immersion liquids

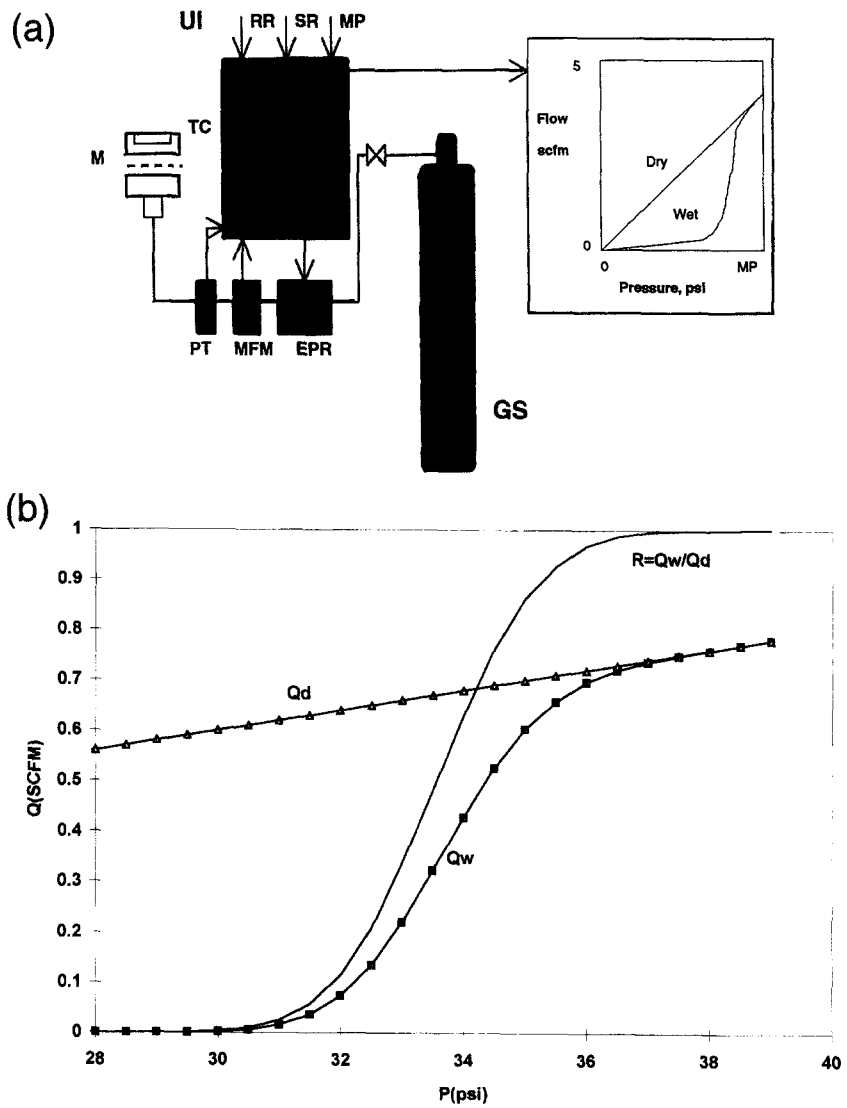

Fig. 2. (a) Schematic diagram of the (g–l) porosimeter used in this study: UI, user inputs; RR, pressure ramp rate; SR, sampling rate; MP, maximum pressure; CU, control unit; EPR, electronic pressure regulator; MFM, mass flow meter; PT, pressure transducer; TC, test cell; M, membrane; GS, gas source. The upstream mass dry flow of air was measured first, the membrane was then wetted with IPA, and this was followed by measurement of the wet flow. (b) Typical data output of a (g–l) porosimetry experiment. Q_d is mass flow rate through a dry membrane; Q_w is mass flow rate through a wet membrane; R ratio of wet/dry flows, P is transmembrane pressure. These data (extrapolated to $p = 0$) were obtained with membrane B in the upstream orientation.

exhibit interfacial (surface) tensions roughly in the range of 15–73 dyn/cm. It is advisable to select a fully-wetting liquid with a zero contact angle, low viscosity, and low volatility that does not alter the membrane in any appreciable way (e.g. by swelling or a chemical attack). A simplified sketch of a two-phase flow through a membrane pore is shown in Fig. 1. An idealized straight cylindrical pore (shown on the left) is characterized by a diameter, d, and length, l. The latter quantity is equal to membrane thickness. Liquid A is the wetting (expelled) phase, while fluid B (air in our case) is the phase intruding the pore at an imposed pressure, P. Due to meniscus curvature and interfacial tension, a pressure differential, $P_1 - P_2 = \Delta P$, develops at the interface. According to de Laplace–Young equation (published in 1805), for a hemispherical meniscus, ΔP relates to γ and d as:

$$\Delta P = (4\gamma/d)\cos\theta \tag{1}$$

where θ is the receding contact angle between phase A and the pore wall. For a fully wetting liquid, $\cos\theta = 1$. A more complicated case involving a non-spherical meniscus was considered by Adamson [4]. Eq. (1) expresses a condition of mechanical (force) equilibrium at the curved interface. For intrusion of phase B (air) to occur, the pressure differential, ΔP, has to be larger than $(4\gamma/d)\cos\theta$. The right side of the sketch in Fig. 1, shows schematically a convoluted path of an air bubble travelling through the maze of a disordered membrane structure. Such "maze path" has been considered previously by Williams and Meltzer [14,15]. It reflects the fact that the air flow through a liquid-filled node-and-throat-type structure follows a convoluted chain of throats (apertures or necks) that open at a given value of $\Delta P = (4\gamma\cos\theta)/d$. The maze path length, L, is considerably longer than the membrane thickness, l. This is usually expressed by pore tortuosity, τ, defined as

$$\tau = L/l \tag{2}$$

Such maze paths represent effective pores that are explored by porosimetry. Even a simplified model of pore size distribution has to consider distributions of both L and the minimum aperture diameters along the path, d(min).

A typical (g–l) porosimetry experiment consists of: (a) measuring upstream air mass flow through a dry membrane as a function of increasing pressure, $Q_d(P)$; (b) immersing the membrane in a wetting liquid; (c) measuring upstream air mass flow through the wet membrane as a function of increasing pressure, $Q_w(P)$ (see insert in Figs. 2a and 2b). The experiments are usually performed with automated porosimeters of the kind described in the Experimental section (Fig. 2a). Computer-controlled instruments with software-driven experiment execution, data acquisition, processing, storage, and plotting are now commercially available. These are, for example, the Porometer™ series instruments marketed by Coulter Electronics, Hialeah, FL, USA, or the complete filter analyzer available from Porous Materials, Inc., Ithaca, NY, USA. The regression-smoothed mass flow–pressure data are used for calculations of a flow ratio, $R(P) = Q_w(P)/Q_d(P)$, its derivative with respect to pressure, $dR(P)/dP$, and different kinds of bubble points (initial, mean, peak bubble point, etc.). In several reports [16–20], this analysis was extended to computation of pore diameter (or radius) distribution functions from $R(P)$, using simplified theoretical models. An alternative method was proposed a long time ago by Grabar and Nikitine [21]. It used the $Q_w(P)$ data alone for computing a "number fraction distribution function" of pore radii, $f(r)$ (in units of inverse length):

$$f(r) = C(dQ_w(P)/dP - Q_w(P)/P)P^5 \tag{3}$$

where C is a proportionality constant. This method was based again on the cylindrical pore model, use of Eq. (1), and the well-known Hagen–Poiseuille equation for laminar flow, Q, of an incompressible fluid of viscosity, η, through a cylindrical pore of radius, r, and length, L, with a zero (gauge) back pressure:

$$Q = (\pi r^4 P)/(8\eta L) \tag{4}$$

For such a model:

$$C = \eta L/(4\pi\gamma^5) \tag{3a}$$

Note that the quantity L is assumed to be constant in Eqs. (3) and (3a). The published methods for computation of pore size distribution functions are controversial for the following reasons: (a) lack of quantitative applicability of Eq. (1) and the flow equations to

disordered stochastic media; (b) lack of reliable calibration methods [3]; (c) difficulties with description of pore dimensions by a single variable (as discussed above); and some uncertainties about the nature of the gas flow. However, the single most important issue is the non-equilibrium character of the (g–l) porosimetry experiment that has been completely ignored in the previously cited reports [16–21]. Kinetic effects (often called "transport properties") frequently complicate measurements that are based on static equlibrium principles (e.g. scanning calorimetry, phase transition measurements, partition chromatography, etc.). In (g–l) porosimetry, the time-dependent factors are usually associated with finite times required to vent tortuous pores (hydrodynamic conduits). The non-equilibrium effects were probably first observed, described and analyzed (in German) by Bechhold et al. [22]. To uphold validity of Mark Twain's aphorism that "oblivion is the only earthly certainty" (next to death and taxes, of course), this seminal work seems now to be safely buried on the yellowing pages of Kolloid Zeitschrift (1931). In our Discussion, we will attempt a partial resuscitation of the section of "Porenweite von Ultrafiltern" [22] (written by one of the co-authors, Schlesinger) that relates to time-dependent effects in two-phase porosimetry. It is demonstrated below, by experiments and theoretical analysis, that the kinetic effects are far from negligible, and that they have to be properly accounted for in the analysis of (g–l) porosimetry data.

It should be mentioned that this study is concerned primarily with the automated (g–l) porosimetry measurements, as practiced today in industrial testing of MF membranes. The automated instrument is not suited for more thorough and lengthy equilibrium-type experiments which would be more appropriate for fundamental investigation.

2. Experimental

Characteristics of the two membranes used in this study, A and B, are summarized in Table 1. As seen, both were ~ 0.2 μm-rated MF membranes of the same overall thickness. Membrane A was an isotropic cellulose diacetate (CA) membrane, while membrane B was a composite (anisotropic) polyvinylidene fluoride (PVDF) membrane with a thin (~ 7 μm) retentive top layer.

The (g–l) porosimeter used in this study was designed and constructed by Tuccelli of Millipore Corp. It is shown schematically in Fig. 2a. The instrument is controlled by a PC-type control unit (PU) that allows the operator to choose pressure ramp rate, ρ (RR in Fig. 2a), within a 0.05–2.0 psi/s range, sampling rate (SR) in number of recorded points per second (0.4–1.6 points/s in this work), and maximum pressure (MP) that typically does not exceed 150 psi. Higher sampling rates are used with faster pressure ramping to generate enough points for reliable curve fitting. The electronic pressure regulator (EPR) consists of a current/pressure (I/P) transducer, and a volume booster. A continuous, linear, smooth, and reproducible pressure ramping is controlled by the PU. The upstream test loop contains a fine air filter (not shown in Fig. 2a), a mass-flow meter (MFM) of a hot-wire anemometer type, and a pressure transducer (PT). The MFM sensor records air flow in SCFM (standard cubic feet per minute), and the PT sensor monitors transmem-

Table 1
Characteristics of membranes used in this study

Membrane	Type	Rating (μm)	Material	Thickness (μm)	IPA visual BP (psi)	Water flux (l m h/psi)
A [a]	Isotropic	0.2	CA	124	19.2	903
B [b]	Composite, anisotropic	0.22	PVDF	124	19	980
B bottom layer	Isotropic	0.65	PVDF	117		5000
B top layer	Anisotropic	0.22	PVDF	7		

[a] Sartorius SM11127, lot no. 20838. Virtually identical pore size distributions of the two surfaces and cross-section were determined by SEM-image analysis [6]. Bulk porosity = 68.9%.

[b] Machine cast by Tkacik [25] on Millipore Durapore DVXA. Retention of 0.15 μm polystyrene (PS) beads, $41 \pm 8\%$; of 0.25 μm PS beads, $98.6 \pm 0.8\%$.

brane pressure in psi (downstream space is at the gauge pressure $P = 0$). The MFM is positioned upstream of the tested membrane to avoid fire hazards and sensing interference by wetting liquid vapors. The test cell design allows use of 25 mm or 47 mm diameter membrane disks. Only 25 mm disks were used in this study. Liquid A was a reagent grade isopropanol (IPA) purchased from Aldrich Chemical Co., with $\gamma = 21.7$ dyn/cm. The experiment itself was described in Introduction. A typical data output is shown in the inset of Fig. 2a, and in more detail in Fig. 2b, where actual data (extrapolated to $\rho = 0$ psi/s) for membrane B in the upstream orientation are shown. The PU stores the smoothed dry and wet flow curves, $Q_d(P)$ and $Q_w(P)$. Subsequently, it computes the ratio $R(P) = Q_w(P)/Q_d(P)$, its first derivative, dR/dP, and the initial and peak bubble point values, P_i and P_p. All experimental results are plotted and printed in a format selected by the operator.

3. Results

The important variable to consider in evaluation of (g–l) porosimetry data is the applied pressure ramp rate, $\rho = dP/dt$. The extremes of ρ (0.05 and 2.0 psi/s) correspond to a forty-fold difference in scan time, t (e.g., 25 or 1000 s to reach 50 psi). Not surprisingly, operators prefer to use shorter scan times (higher ramp rates), especially when a heavy load of samples is to be analyzed. The Coulter Porometer II manual [16] specifies scan times below 600 s. To reach the specified maximum operating pressure of 195 psi, selected value of ρ has to be higher than 0.325 psi/s. Before we present the experimental data on the effect of ρ on $dR(P)/dP$, i.e. the usual "end result" of the (g–l) porosimetry analysis, we want to consider two other points. The first deals with response times of the two upstream detectors: the pressure transducer and the mass flow meter. The response times are both in the range below 1 ms, and we may regard them as instantaneous for our purposes. The second point to consider is the effect of ρ on the upstream-measured mass flows. It can be readily shown that for air at $T = 298.3$ K (25°C) and below $P = 100$ psi (690 kPa), the ideal gas equation of state does not deviate significantly from the more accurate van der Waals or virial expansion equations. Differentiation of the ideal gas equation of state with respect to time, and

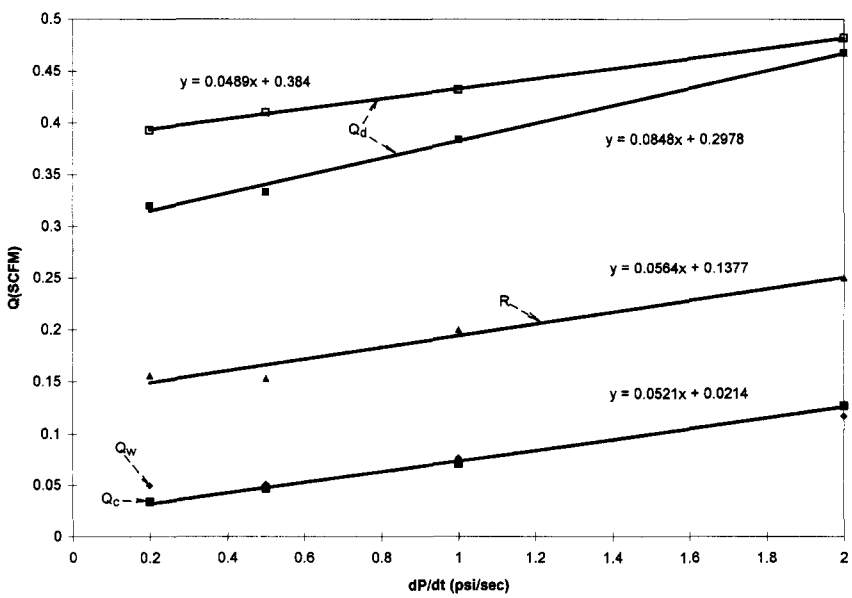

Fig. 3. Pressure ramp rate, dP/dt, dependence of mass air flows, Q, measured with membrane A at $P = 20$ psi. The symbol definition is the same as in Fig. 2b. A "compressive" flow, Q_c, was determined with an air-impermeable Mylar film in the test cell. Straight-line regression equations are given for each set of points.

for a constant volume of the upstream air space, V, yields:

$$(dn/dt)_V = (V/RT)(dP/dt)_V = (V\rho)/(RT) \quad (5)$$

where R is the universal gas constant (8.314 J K^{-1} mol^{-1}), T is the absolute temperature in K, and n is the number of moles of air. The molar flow, dn/dt, is measured by the mass flow meter (1 (standard cubic foot)/min = 1 SCFM = 1.264 mol/min for an ideal gas at $T = 273.2$ K and P(absolute) = 14.7 psi). Using the engineering units employed by our instrument, we can rewrite Eq. (5) in the form:

$$Q_{in}(\text{SCFM}) = 5.975V(\text{ft}^3)\,\rho(\text{psi/s}) \quad (6)$$

where Q_{in} is the air flow (at $T = 298.2$ K) through the upstream positioned flow meter. The unknown upstream air space volume, V, was obtained by measurements of a "compressive" mass flow, Q_c, using an air-impermeable Mylar film in the test cell instead of a membrane. When we plotted Q_c values at $P = 20$ psi against ρ (large filled squares in Fig. 3), we obtained a straight line with a slope of ≈ 0.052 SCFM s psi^{-1}. The small intercept (≈ 0.02 SCFM) is likely due to minor air leaks from the upstream space. A virtually identical set of results (filled diamonds) was obtained by evaluating the effect of ρ on the wet flow, Q_w, measured with membrane A at $P = 20$ psi, i.e. at the initial bubble point. This measurement was carried out by a different operator on a different day. The slope value yielded $V = 8.7 \times 10^{-3}$ $ft^3 = 246$ cm^3. A dry mass flow, Q_d, dependence on ρ is slightly more complicated. Ideally, we should obtain:

$$Q_d(\text{SCFM})_{in} = Q_d(\text{SCFM})_{out} + 0.052\rho \quad (7)$$

where the subscript "out" refers to the downstream mass flow. Measurements of dry flow–pressure curves, $Q_d(P)$, at different values of ρ, revealed that they were significantly more non-linear (concave upward) at low values of ρ. The same trends were observed with membrane B in both orientations. One possible explanation is that membrane hydraulic resistances were more variable during longer scans at low values of ρ. The uncorrected data for $Q_d(\rho)$ with membrane A (small filled squares in Fig. 3) yielded an unexpectedly high slope value of ≈ 0.085 SCFM s psi^{-1}. After correction for nonlinearity of the $Q_d(P)$ data (open squares in Fig. 3), the slope value became ≈ 0.049 (within 6% of the expected value). The corrections were made by drawing straight lines between Q_d values at $P = 0$ psi and

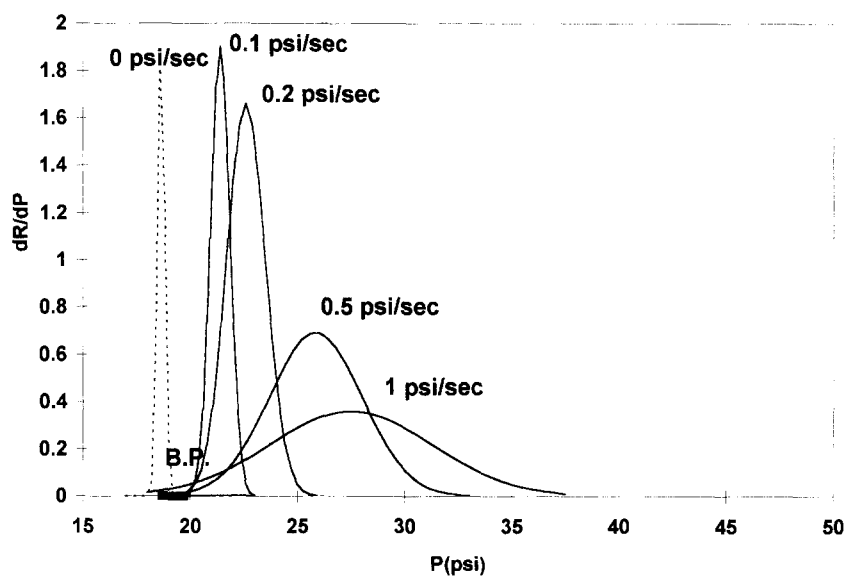

Fig. 4. Pressure ramp rate effects on the dR/dP vs. P curves measured with an isotropic membrane A. Ramp rate values are given for each curve. A curve extrapolated to $\rho = 0$ psi/s (dashed line), and the error range for visual bubble points, BP, determined by a manual method (thick solid line) are also shown.

the end points (usually at MP = 50 psi). The purpose was to establish that the $Q(\rho)$ dependence for both wet and dry flows can be explained by the ideal gas behavior, Eqs. (5) and (6). A moderate dependence of R on ρ (filled triangles in Fig. 3) is mainly due to the large intercept of the $Q_d(\rho)$ function. This applies only to regions below initial bubble points, P_i. Once the membrane becomes fully vented at pressure P_v, $Q_w = Q_d$, and R remains independent of ρ. Examination of experimental data showed that the more important first derivative values, $dR(P)/dP$, were consistently zero (independent of ρ) below P_i and above P_v. This suggests that the effects of the upstream "compressive" mass flow on $dR(P)/dP$ are negligible.

However, the wet flow curve is dramatically influenced by the pressure ramp rate for a different reason, namely finite flow rates of the expelled liquid. The effect is demonstrated by the experimental curves of dR/dP vs. P (Figs. 4–6) that were measured at different values of ρ. In Fig. 4, data obtained with membrane A, an isotropic 0.2 μm-rated cellulose acetate membrane (Sartorius SM 11127) are presented. Measurements were carried out with pressure ramp rates, $\rho = 0.1$, 0.2, 0.5, and 1.0 psi/s. The experimental points were fitted by normal (Gaussian) distribution functions, characterized by values of mean (or median), P_m, and standard deviation, σ. The heights of the peaks, $K = (dR/dP)_m$, in arbitrary units reported by the instrument were proportional to the actual values in psi^{-1}. Each curve was thus defined by a three-parameter equation:

$$(dR/dP) = K \exp\left(-(P - P_m)^2/(2\sigma^2)\right) \qquad (8)$$

Values of K, P_m, and σ were extrapolated to $\rho = 0$ psi/s, using regression analysis. For values of P_m, a better linear fit was obtained with $P_m = P_m(\sqrt{\rho})$. The other two parameters were extrapolated by a straight-line regression of (K or σ) vs. ρ points. Obviously, with only four points used in each regression, the extrapolation has to be viewed as only approximate. In spite of that, a clear trend was observed for dependence of both P_m and σ on ρ. Therefore, we used the extrapolated values for calculation of a dR/dP vs. P curve expected at $\rho = 0$ (drawn in dashed line). Fig. 4 shows also the range (19.2 ± 0.5 psi) of visual bubble points (thick line) measured independently by a manual method.

Fig. 5 shows analogous smoothed data obtained with membrane B (an anisotropic composite PVDF

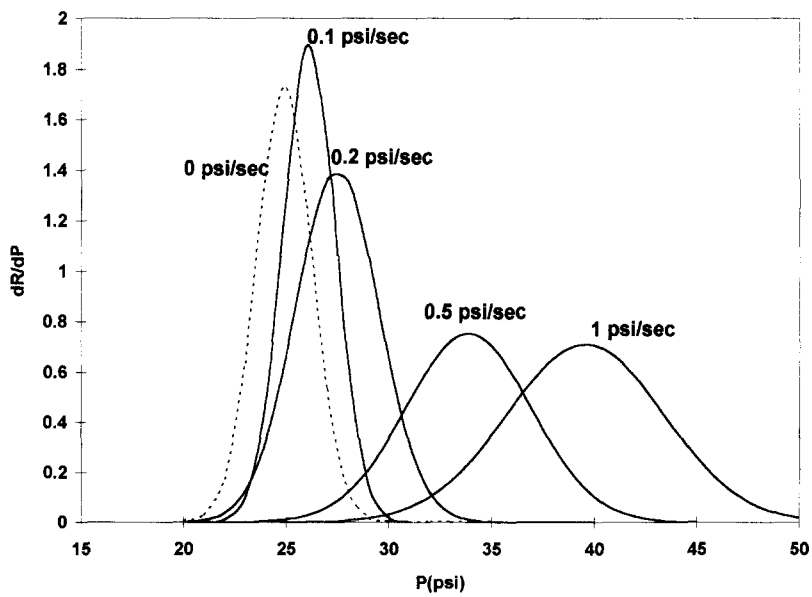

Fig. 5. Data analogous to those shown in Fig. 4, measured with an anisotropic (composite) membrane B in downstream orientation (explained in the text).

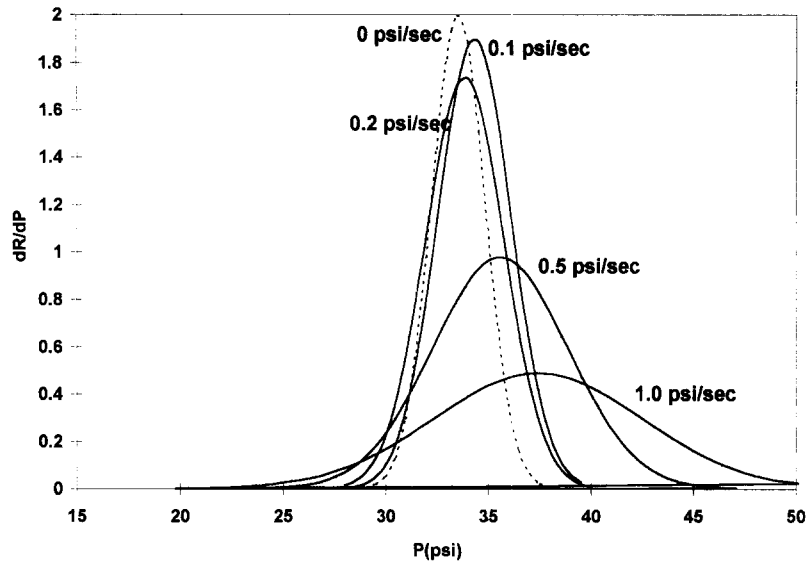

Fig. 6. Data analogous to those shown in Fig. 4, measured with an anisotropic membrane B in upstream orientation.

membrane). With this membrane, the results depended markedly on the sample orientation in the test cell. Data shown in Fig. 5 were obtained with the open (belt) side of the membrane facing intruding air. For brevity, we refer to this orientation as "downstream", indicating that the tight (more retentive) side faced the downstream part of air flow. Extrapolation of the peaks to $\rho = 0$ psi/s was done in the analogous way as with the peaks in Fig. 4.

Fig. 6 shows the ramp rate effects observed with membrane B in the "upstream" orientation. Note that the effect of membrane orientation was considerably more pronounced at low values of ρ. The missing variable in Figs. 4–6 is scan time, t. In Fig.

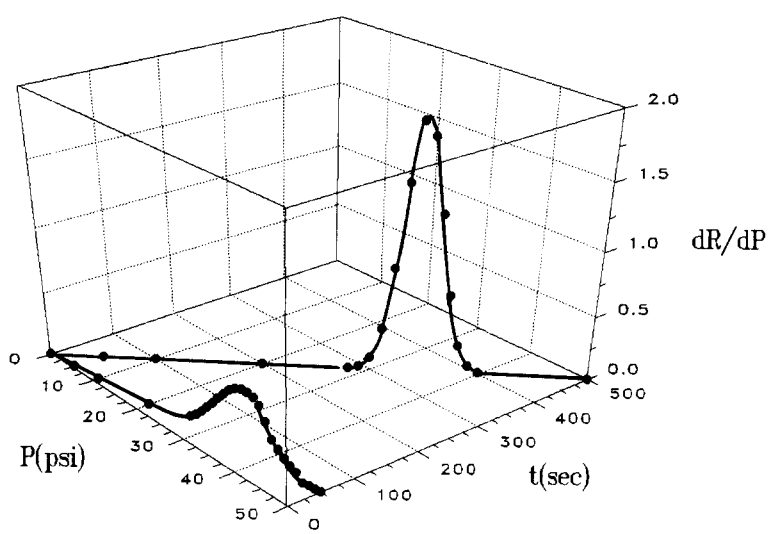

Fig. 7. Two dR/dP curves from Fig. 6 [at $\rho = 0.1$ (rear) and 1.0 (front) psi/s] redrawn in 3D coordinates to show their pressure and time dependence.

Table 2
Parameters of dR/dP vs. P curves shown in Figs. 4–6

Membrane A			Membrane B			
			Upstream		Downstream	
Ramp rate (psi/s)	P_m (psi)	σ (psi)	P_m (psi)	σ (psi)	P_m (psi)	σ (psi)
extrapolation						
0	18.7	0.17	33.6	1.31	24.9	1.36
0.1	21.4	0.45	34.3	1.79	26.1	1.28
0.2	22.6	0.9	33.9	1.91	27.5	2.04
0.5	25.9	2.16	35.6	3.31	33.9	3.06
1	27.5	3.78	37.4	5.09	39.6	3.83
Estimated pore diameter range (μm)						
	0.65–0.69		0.34–0.42		0.43–0.61	
Parameters reported by the porosimeter						
Ramp rate (psi/s)	P_i (psi)	P_p (psi)	P_i (psi)	P_p (psi)	P_i (psi)	P_p (psi)
0.1	20.3	21.2	29.9	34.3	23.2	26.1
0.2	20.7	22.5	29.5	33.9	24.2	27.5
0.5	21.9	25.9	27.9	35.4	26.8	33.9
1	20.5	27.4	28.5	37.4	31.9	39.6
Indicators of peak width						
Ramp rate (psi/s)	ΔP (psi)	σ (psi)	ΔP (psi)	σ (psi)	ΔP (psi)	σ (psi)
0.1	0.9	0.45	4.4	1.79	2.9	1.28
0.2	1.8	0.9	4.4	1.91	3.3	2.04
0.5	4	2.16	7.5	3.31	7.1	3.06
1	6.9	3.78	8.9	5.09	7.7	3.83

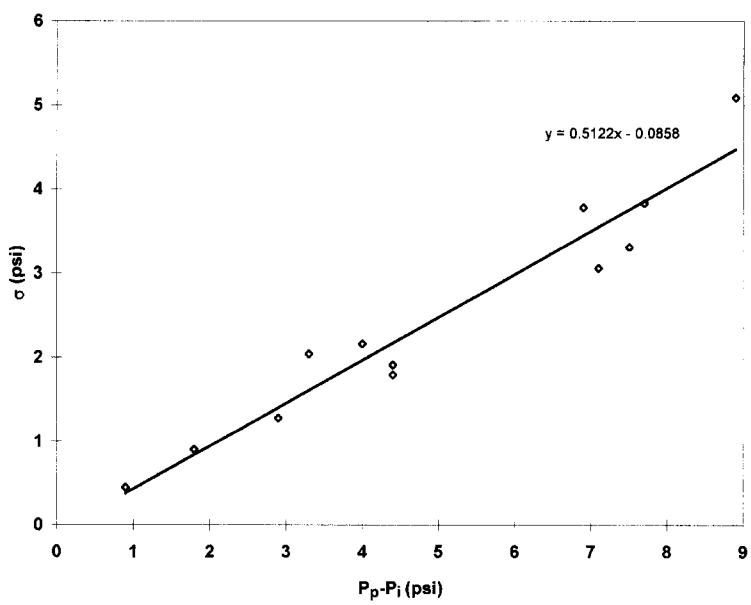

Fig. 8. Standard deviations, σ, of fitted Gaussian peaks plotted against difference of instrument-reported initial and peak bubble points, P_i and P_p. Data were pooled from all three experiments. The straight-line regression equation is shown.

7, two curves from Fig. 6 (for $\rho = 0.1$ and 1.0 psi/s) were plotted in a 3D graph that shows also the time axis. This illustrates the point that dR/dP is a function of at least two independent variables (P and ρ, or P and t).

All values of P_m and σ used in Figs. 4–7 (including those extrapolated to $\rho = 0$) are summarized in Table 2. Since not all experimental curves were perfectly Gaussian, the fitted parameters P_m and σ were compared with the initial and peak bubble point values, P_i and P_p, determined by the porosimeter. These values are listed in the middle panel of Table 2. The P_m and P_p data are in agreement within experimental error. The difference, $\Delta P = P_p - P_i$ is indicative of peak width and is proportional to σ. This is clearly illustrated in Fig. 8. It was somewhat surprising to find that ΔP is approximately equal to 2σ, and not the expected 3σ. This was due to a less than perfect fit of experimental points in the vicinity of P_i by more "forward tailing" Gaussian curves. Thus, the curves shown in Figs. 4–7 under represent P_i values roughly by 1σ, i.e. 1–5 psi. This does not change in any important way the main pattern of presented results, or their interpretation. The agreement was considerably better for the trailing edges of the peaks (not shown). For the sake of completeness, the ramp rate dependence of P_p and P_i in all three experiments is plotted in Fig. 9. The trends are basically the same as those illustrated by Figs. 4–6.

4. Discussion

The data presented above raise several interesting questions. Why are the (g–l) porosimetry curves so strongly affected by imposed pressure ramp rates? Why does the extrapolated dR/dP vs. P peak for an irregular stochastic structure like membrane A exhibit width ($6\sigma = 1.0$ psi) that is within the experimental error of bubble point measurements? Why is the expected effect of membrane orientation with an anisotropic membrane B virtually obliterated at higher ramp rates? What is the nature of the air flow, and are we justified in using the Hagen–Poiseuille equation [Eq. (4)] to describe it? Finally, our headline question: are the pore size distributions measurable by (g–l) porosimetry? Below, an attempt is presented to formulate at least partial answers to these questions.

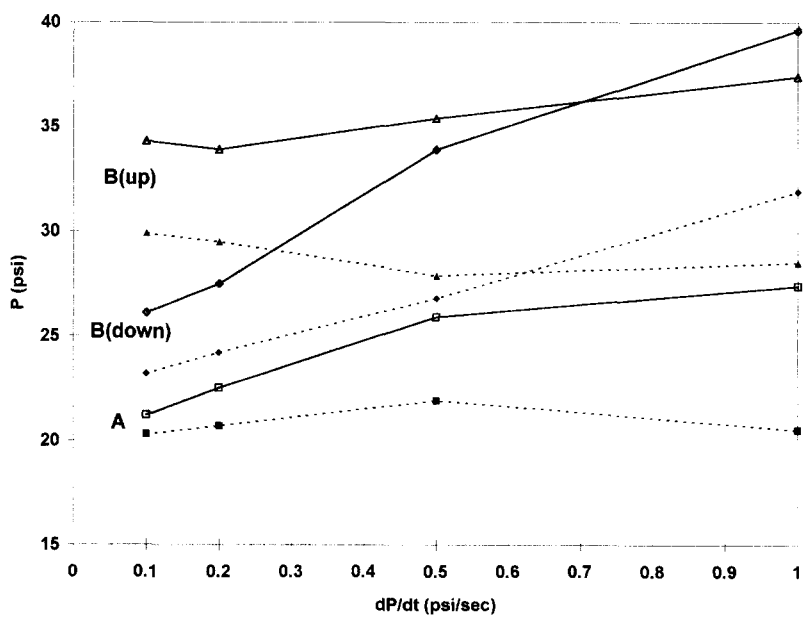

Fig. 9. Initial (filled points) and peak (open points) bubble points, P_i and P_p, plotted as a function of pressure ramp rate. Letters A and B refer to the membrane used, (up) and (down) to membrane orientation in the holder.

4.1. Effect of pressure ramp rate

As mentioned in the Introduction, even a simplified model for pore intrusion in random media has to reflect both a size distribution of restricting orifices (throats), $f(d)$, and a length distribution of tortuous maze paths, $f(L)$. To keep things simple (hopefully not oversimplified), we will model the maze path as a tortuous cylindrical conduit, characterized by an effective diameter, $d = 2r$, and an effective tortuous length, L. According to Eq. (4), hydraulic resistance for laminar viscous flow through a cylindrical capillary is proportional to L/d^4. We can then incorporate other resistance contributing factors such as the effects of convolution, convergent–divergent character of the conduit pore, surface roughness, etc., into L. This will make the "effective" L larger than its actual geometric length. This simplification is justified only if the above mentioned effects do not change the nature of the flow.

Let us now recapitulate the theoretical approach of Bechhold et al. [22] that is based on a simple straight pore model, as depicted in Fig. 1. We will use here the effective tortuous pore length, L, rather than the membrane thickness, l. Both fluids A and B are treated as incompressible in [22]. However, Eq. (4) (written for a zero back pressure, $P_1 = 0$), applies also to a compressible fluid B (such as air) for a case where its volume (or flow) is measured at an average pressure in the air-filled part of the capillary, $(P + P_1)/2$. This is true even if $P_1 \neq 0$, but than $(P - P_1)$ appears in Eq. (4) instead of P. The viscosities of A and B are η_A and η_B. The expelled phase A wets the membrane completely, i.e. cos $\theta = 1$. In a time interval dt, displaced volumes, dV, of both fluids are equal and evaluated from Eq.(4):

$$dV = \pi r^2 dx = \left(\pi r^4 (P - P_1) dt\right)/(8\eta_B x) = \left(\pi r^4 P_2 dt\right)/(8\eta_A (L - x)) \quad (9)$$

Therefore:

$$(P - P_1)/(\eta_B x) = P_2/(\eta_A (L - x)) \quad (10)$$

Incorporation of Eq. (1), and rearranging yields:

$$P_2 = (P - 2\gamma/r)/\left(1 + (\eta_B x)/(\eta_A (L - x))\right) \quad (11)$$

We combine now Eqs. (9) and (11):

$$\pi r^2 dx = \left(\pi r^4 (P - 2\gamma/r) dt\right)/\left(1 + (\eta_B x)/(\eta_A (L - x))\right)\left(1/(8\eta_A (L - x))\right) \quad (12)$$

and introduce the pressure ramp rate:

$$\rho = P/t \quad (13)$$

After rearranging, we obtain:

$$8\eta_A L dx + x(\eta_B - \eta_A) dx = r^2 \rho t dt - 2\gamma r dt \quad (14)$$

Eq. (14) is subsequently integrated within limits:

$$0 \leq x \leq L; \text{ and } 2\gamma/(r\rho) \leq t \leq T \quad (15)$$

assuming that pore intrusion starts at time, $2\gamma/(r\rho)$, at which $P = 2\gamma/r$, and ends at time, T. The integration yields a quadratic equation for T:

$$r^2 \rho T^2/2 - 2r\gamma T + \left(2\gamma^2 - 4(\eta_A + \eta_B) L^2\right) = 0 \quad (16)$$

Only the root with a positive sign between the two numerator terms has a physical meaning:

$$T = \left(2\gamma + \left(8\rho(\eta_A + \eta_B) L^2\right)^{0.5}\right)/(\rho r) \quad (17)$$

Employing Eq. (13) and substituting $d = 2r$, we obtain the desired expression for the intrusion pressure, P:

$$P = 4\gamma/d + 8\left((\eta_A + \eta_B)/2\right)^{0.5} L \rho^{0.5}/d \quad (18)$$

This is the Schlesinger–Bechhold equation [22] which introduces dependence of the intrusion (bubble point) pressure, P, on the commonly ignored variables L and ρ. At $\rho = 0$, it reduces to Eq. (1). For IPA–air ($\gamma = 21.7$ dyn/cm; $\eta_A = 2.43 \times 10^{-2}$ P; $\eta_B = 1.8 \times 10^{-4}$ P), it becomes:

$$P\,(\text{psi}) = 12.59/d\,(\mu\text{m}) + 3.372 \times 10^{-3} L\,(\mu\text{m}) \left[\rho\,(\text{psi/s})\right]^{0.5}/d\,(\mu\text{m}) \quad (19)$$

Eq. (19) suggests that the L/d ratio has to be about 1×10^3 to produce an increase of P by 1 psi at $\rho = 0.1$ psi/s. However, L and d have to be considered as two independently distributed structural variables. Their distribution could be expressed by a bivariate distribution function $f(d,L)$. The most hydraulically resistant pores are those with the maximum tortuous length, L_{max}, and the minimum effective diameter, d_{min}. Conversely, the values, L_{min} and

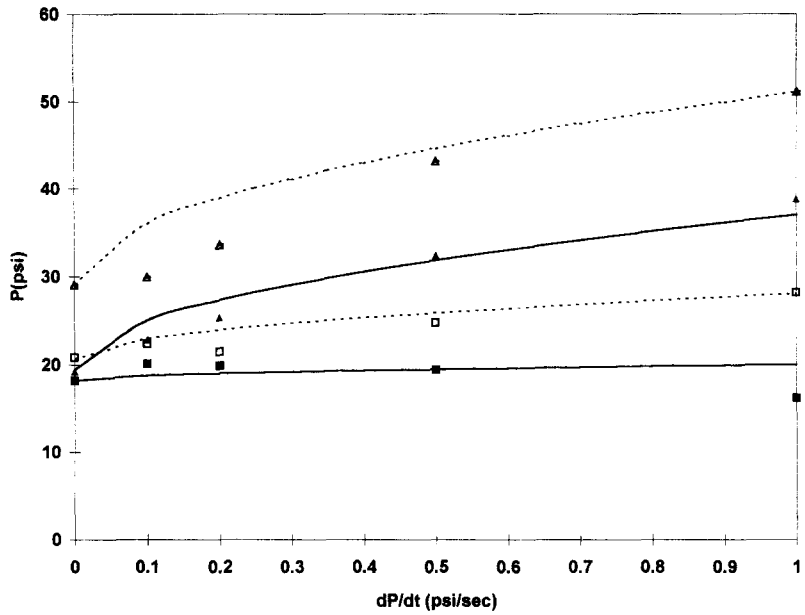

Fig. 10. Data from the experiments shown in Fig. 4 (squares) and Fig. 5 (triangles) compared to curves calculated from the Schlesinger–Bechhold theory [Eq. (19)]. The $P_m + 3\sigma$ values are marked by empty symbols, the $P_m - 3\sigma$ values by filled symbols. Solid line curves apply to the most permeable pores (with lowest L/d value), dashed-line curves to the least permeable pores (with highest L/d value). P_m and σ are the mean and standard deviation of $dR(P)/dt$ curves.

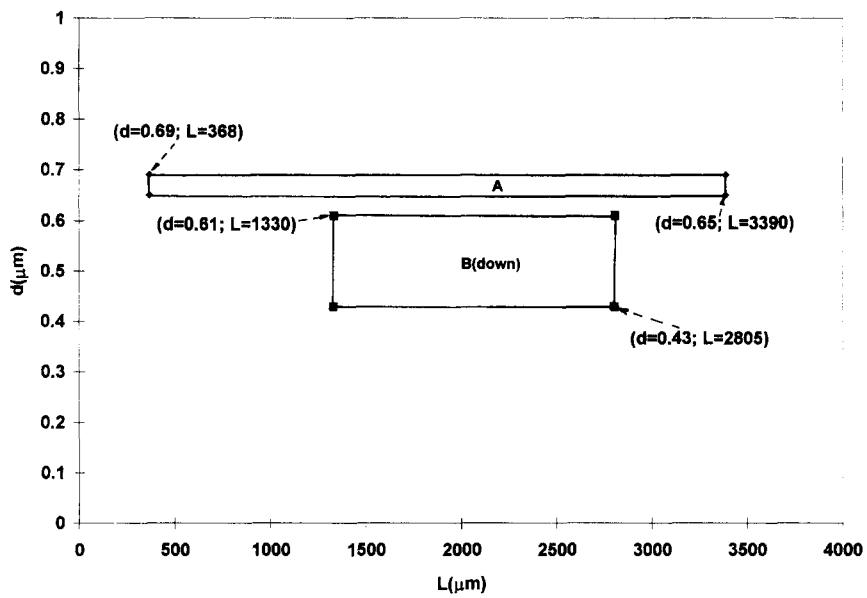

Fig. 11. Ranges of pore diameters, d, and pore lengths, L, used in calculation of the theoretical curves shown in Fig. 10.

d_{max}, apply to the most permeable pores. An estimate of d_{min} to d_{max} range can be obtained from the (g–l) porosimetry data, extrapolated to $\rho = 0$. Eq. (1), with cos $\theta = 1$, is used for P to d conversion. Thus, for membrane A, the extrapolated $P_m \pm 3\sigma$ range (18.2 to 19.2 psi) yielded d_{min} to $d_{max} = 0.65$ to 0.69 μm. This coincides with the range of experimental error in pore diameters evaluated from manual bubble point measurements. Similarly for membrane B in the downstream orientation, the extrapolated $P_m \pm 3\sigma$ range (20.8 to 29 psi) yielded d_{min} to $d_{max} = 0.43$ to 0.61 μm. This range is 4.5 times larger than that determined for membrane A, but still very narrow. Examination of the porosimetry data from these two experiments (Fig. 4, Fig. 5 and, Fig. 9) suggested a reasonable agreement with the Schlesinger–Bechhold equation, Eq. (19). This is shown in Fig. 10, where the $P_m \pm 3\sigma$ points, obtained at four different ramp rates, are compared to curves calculated from Eq. (19). The fitted ranges of d and L are shown in Fig. 11. As seen in Fig. 10, the agreement between theory [22] and experiment was not perfect. It appeared somewhat better for membrane A (filled symbols) than membrane B (open symbols). However, the main two features of the experimental results could be well reproduced by Eq. (19): (a) relative insensitivity of P_i (squares) to an increase of ρ; (b) pronounced increase of peak width, 6σ, with increasing ρ.

The results obtained with membrane B in the upstream orientation (Fig. 6, Fig. 9, and Table 1) are more puzzling. The P_i values were found to be decreasing with increasing ρ, the P_m (or P_p) values were almost independent of ρ, and the σ (or ΔP) values increased with increasing ρ. At low ρ, the bubble point range was clearly higher than that measured with the same membrane in the downstream orientation. However, at $\rho = 0.5$ and 1.0 psi/s, the sensitivity to orientation was virtually obliterated. Clearly, the results obtained with membrane B in the upstream orientation cannot be fitted to Eq. (19). In the absence of a better explanation, we can reason that Eqs. (1) and (4), from which Eqs. (18) and (19) are derived, do not apply to venting of pore space in a very thin (~ 7 μm) top layer of a composite membrane, when this layer faces intruding

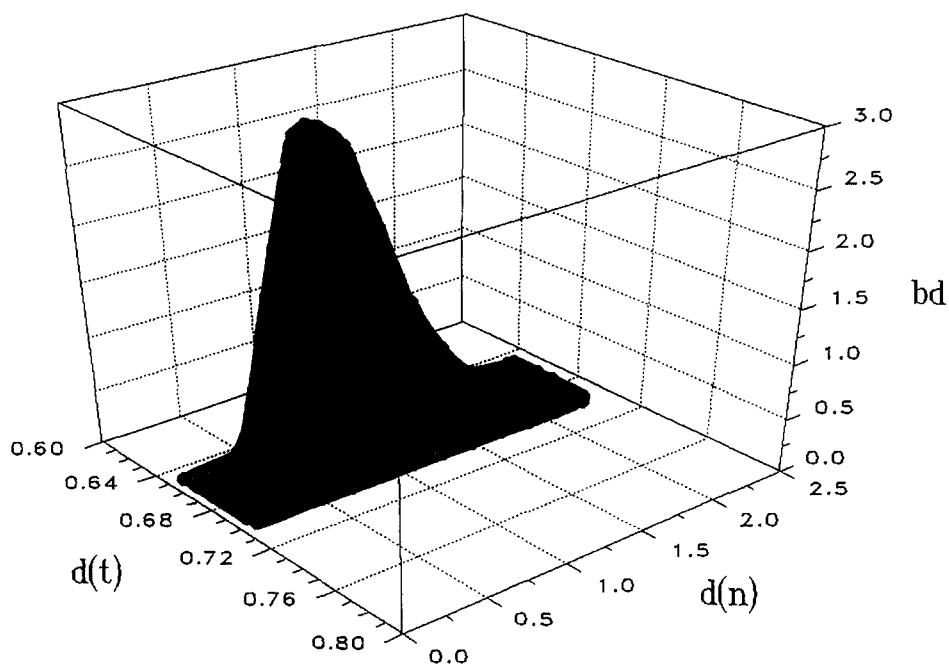

Fig. 12. Bivariate pore diameter distribution function, *bd*, for membrane A. The 3D surface shows distribution of uncorrelated node-type pore diameters, $d(n)$, from SEM-image analysis [6], and throat-type pore diameters, $d(t)$, from (g–l) porosimetry (this work).

air directly. The length of vented conduits is likely comparable to their width, and entrance flow effects may be significant.

4.2. Narrow width of pore diameter distributions evaluated from (g–l) porosimetry

As demonstrated above, the (g–l) porosimetry peaks have to be extrapolated to zero pressure ramp rate in order to eliminate interference from kinetic effects. The extrapolated $P_m \pm 3\sigma$ data, in conjunction with Eq. (1), allow us to estimate diameter ranges of intruded (characterized) pores. These ranges are also listed in Table 2 (second panel). They are surprisingly narrow, particularly for membrane A. Since the porosimetry data were well fitted by symmetric normal (Gaussian) distribution curves, we can assume that the flow-weighted diameter distributions are also close to Gaussian. This result is in striking contrast to the wide and asymmetric pore size distribution determined previously for membrane A by the SEM (scanning electron microscopy)-image analysis method [6]. Our interpretation is that the larger pores, with highly variable diameters, d(n), observable by SEM on the surface of a membrane, are mainly the "node-type" pores. On the other hand, pores characterized by (g–l) porosimetry (a pore-intrusion method) are mainly "throat-type" pores with much less variable diameters, $d(t)$. If we assume that the diameter distribution functions, $f(d(n))$ and $f(d(t))$, for these two classes of pores are uncorrelated, we can follow the suggestion of Dullien [13], and calculate a bivariate distribution function, $bd(d(n),d(t))$. Such a function is defined as:

$$bd(d(n)),\ d(t)) = f(d(n))f(d(t)) \qquad (20)$$

The bd function is shown graphically in Fig. 12. The maximum height of the log-normal function, $f(d(n))$, was adjusted to match that of the normal distribution function, $f(d(t))$. Fig. 12 illustrates clearly a remarkable size disparity between the two pore populations.

4.3. Nature of flow in (g–l) porosimetry

The kinetic effect, as expressed by the second term in Eq. (18), is caused mainly by a relatively slow flow of the expelled liquid. This is due to a great difference between viscosities of the two fluids: $\eta(\text{IPA}) = 2.43 \times 10^{-2}$ Poise and $\eta(\text{air}) = 1.80 \times 10^{-4}$ Poise. The latter value is virtually negligible in Eq. (18). The upper bound for liquid flow velocity, v, at $P = 50$ psi through the most permeable pore ($d = 0.7$ μm, $L = 370$ μm) is about 0.6 cm/s, corresponding to a Reynolds number, Re, on the order of 7×10^{-4}. Although the transition region of Re for flow turbulence is lowered in convergent–divergent conduits [23], it appears safe to conclude that the liquid flow through MF membrane "pores" is laminar. During liquid expulsion, flow of air, with a higher kinematic viscosity of $\approx 1.5 \times 10^{-1}$ cm^2/s (compared to $\approx 3.1 \times 10^{-2}$ cm^2/s for IPA), and $Re \approx 1.4 \times 10^{-4}$, is also laminar. Even for the fastest, slip-corrected (see below), dry membrane air flow, the maximum value of "pore" Re is comfortably low, on the order of 5×10^{-2}. Therefore, assumption of laminar flows, permitting use of Eqs. (4) or (22) for the modeled cylindrical conduits is justified.

The applicable mechanism of air flow is important for proper evaluation of pore diameter distribution functions [19]. If a continuum viscous flow, described by the Hagen–Poiseuille equation, Eq. (4), applies, the wet/dry flow ratio, $R(P)$, can be expressed as:

$$R(P) = \left(\int_{d_{max}}^{d} f(d)\, d^4 dd\right) \Big/ \left(\int_{d_{max}}^{d_{min}} f(d)\, d^4 dd\right) \qquad (21)$$

where $f(d)$ is the number fraction distribution function, $d = (4\gamma \cos\theta)/P$ from Eq. (1), and d_{min}, d_{max} are the extremes of the pore diameter distribution. The $R(P)$ curve (shown, for example, in Fig. 2b) is a cumulative flow-weighted distribution function, and $dR(P)/dP$ corresponds to its differentiated (probability density) form.

The applicable mechanism of air flow depends on the value of Knudsen number, $K = 2\lambda/d$, where λ is the mean free path of gas molecules (about 66 nm for air under our experimental conditions). A fully developed Knudsen (free-molecular) air flow, considered in [19] occurs at values of $K > 10$ [24], and it is unlikely that it plays important role with the studied MF membranes. However, it has to be certainly considered for gas flow through UF membranes. The range of $0.2 < 0.4$, applicable to our experiments, straddles so called "dilute" ($K = 0$–

0.25) and "transition" ($K = 0.25$–10) regions of gas flow. Under these conditions, the viscous flow is likely enhanced by diffusional reflection from conduit walls. This effect is usually [24] accounted for by a so-called "slip correction factor", $(1 + 3.99K)$, that changes Eq. (4) (with $d = 2r$) into:

$$Q = (1 + 3.99K)\pi d^4 P/(128\eta_B L) \qquad (22)$$

However, both λ and d(intruded) are proportional to $1/P$. Over a relatively narrow range of P and d in our experiments, K can be regarded as a constant. Therefore, the slip correction does not alter significantly Eq. (21). Both wet and dry flows of air are proportional to d^4.

The previously mentioned method of Grabar and Nikitine [21] allows evaluation of a number fraction distribution function, $f(d)$, from wet flow data by means of Eq. (3). In derivation of Eqs. (3) and (3a), a purely viscous flow [Eq. (4)], and L = constant were assumed. Therefore, the method applies only to $Q_w(P)$ data extrapolated to $\rho = 0$. In Fig. 13, we compare pore diameter distribution curves, (dR/dP) vs. d, and $f(d)$ vs. d [21] calculated from data shown in Fig. 2b. These data correspond to the ($\rho = 0$ psi/s) curve shown in Fig. 6 (membrane B; upstream orientation), and an extrapolated ($\rho = 0$ psi/s) relationship, Q_d (SCFM) $= 0.02P$ (psi). As expected, and also shown in Fig. 13, the flow-weighted distribution curve (solid line) is positioned to the right of the number fraction distribution curve (dashed line). The (dR/dP) curve was normalized to yield $R = 1$ at P_{max} (Fig. 2b). The $f(d)$ curve was normalized to the same height as the other curve. In view of the narrow width of these distributions, the observed difference between the two curves is very small. For wider distributions of d, the difference can be substantial [4,19]. In Fig. 13, the $f(d)$ curve is slightly asymmetric (non-Gaussian).

5. Conclusions

5.1. Are pore size distributions in MF membranes measurable by two-phase flow porosimetry?

The answer is a qualified and limited yes. In recapitulation of the reported findings, we list below the qualifying conditions.

(a) The (g–l) porosimetry data have to be extrapo-

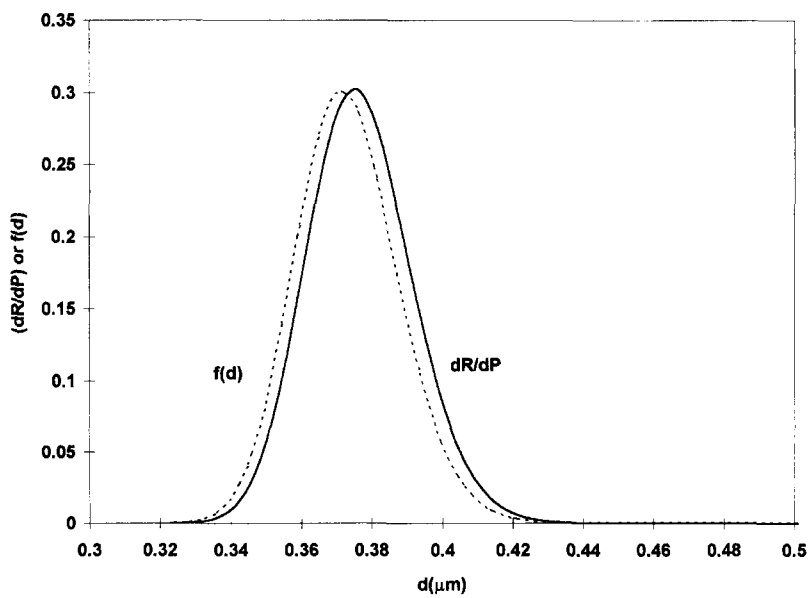

Fig. 13. Pore diameter, d, distribution curves calculated from the data shown in Fig. 2b (membrane B, upstream orientation, $\rho = 0$). The flow-weighted distribution, dR/dP (solid line) and the number fraction distribution, $f(d)$, [21] (dashed line) are compared. To convert P into d, Eq. (1) (with $\cos\theta = 1$) was used.

lated to zero pressure ramp rate to eliminate interfering kinetic effects, or (if possible) obtained at $\rho = 0$.

(b) The calculated pore diameter distributions refer to those of cylindrical pore "equivalents", and not any "real geometry" pores.

(c) The characterized pores are of a "throat type". They are (on average) smaller and considerably less variable in size than the "node-type" pores visualized by SEM.

(d) A distinction has to be made between the flow-weighted distribution, $dR/dP(d)$, and the number fraction distribution, $f(d0)$ [21]. For narrow distributions, the two functions are very similar. For wider ranges of d, they are significantly different. Both distributions are directly obtainable from experimental data (extrapolated to $\rho = 0$), if C in Eq. (3a) is regarded as an adjustable proportionality constant.

(e) The observed conspicuous ramp rate dependence of (g–l) porosimetry peaks can be ascribed to a distribution of tortuous pore lengths, and interpreted in terms of the Schlesinger–Bechhold theory [22]. This approach did not work for a composite membrane with the retentive layer facing intruding air (i.e. in the "upstream" orientation).

Acknowledgements

The author gratefully acknowledges valuable contribution and inputs of Gabriel Tkacik to this work. Ronald Tuccelli, who designed and constructed the instrument used, provided also useful information and suggestions.

References

[1] H. Bechhold, Permeability of ultrafilters, Z. Phys. Chem., 64 (1908) 328–342 (in German).
[2] A. Einstein and H. Muehsam, Experimental determination of pore size in filters, Deut. Med. Wochsch., 49 (1923) 1012–1013 (in German).
[3] L. Zeman and A. Zydney, Microfiltration and Ultrafiltration: From Principles to Successful Applications, Marcel Dekker, NY, 1996, Chapt. 4.
[4] A.W. Adamson, Physical Chemistry of Surfaces, 3rd edn., Wiley, NY, 1976, pp. 4–6
[5] J.D. Ferry, Chem. Rev., 18 (1936) 373.
[6] L. Zeman and L. Denault, Characterization of MF membranes by image analysis of electron micrographs. Part I. Method development, J. Membrane Sci., 71 (1992) 221–231.
[7] L. Zeman, Characterization of MF membranes by image analysis of electron micrographs. Part II. Functional and morphological parameters, J. Membrane Sci., 71 (1992) 233–246.
[8] H. Yasuda and J.T. Tsai, Pore size of microporous polymer membranes, J. Appl. Polym. Sci., 18 (1974) 805.
[9] F.W. Altena, H. Knoef, H. Heskamp, D. Bargeman and C.A. Smolders, Some comments on the applicability of gas permeation method to characterize porous membranes, J. Membrane Sci., 12 (1983) 313–322.
[10] A. Botino, G. Capannelli, P. Petit-Bon, N. Cao, M. Pegoraro and G. Zoia, Pore size and pore size distribution in MF membranes, Sep. Sci. Technol., 26 (1991) 1315–1327.
[11] D.B. Pall, Quality control of absolute bacterial removal filters, Bull. Parenteral Drug. Assoc., 29 (1973) 192–204.
[12] A.R. Reti, An assessment of test criteria for evaluating performance and integrity of sterilizing filters, Bull. Parenteral Drug. Assoc., 31(4) (1977) 187–194.
[13] F.A.L. Dullien, Determination of pore accessibilities. An approach, J. Petrol. Technol., 21 (1969) 14–15.
[14] R.E. Williams and T.H. Meltzer, Membrane structure, the bubble point, and particle retention: a new theory, Pharm. Technol., 7(5) (1983) 42–44.
[15] T.H. Meltzer, Filtration in the pharmaceutical industry, Adv. Parenteral Sci., 3 (1987) 123.
[16] Operator's Manual, Coulter Porometer II, Coulter Corp., Hialeah, FL, USA, 1990
[17] R.W. Lines, A pore man's guide, Filtration News, (1992) 40–42.
[18] C.T. Badenhop, A.T. Spann and T.H. Meltzer, Consideration of parameters governing membrane filtration, in J.E. Flinn (Ed.), Membrane Science and Technology, Plenum, NY, USA, 1970.
[19] P. Schneider and P. Uchytil, Liquid expulsion permporometry for characterization of porous membranes, J. Membrane Sci., 95 (1994) 29–38.
[20] A.J. Thomas, H.H. Duerrheim and M.J. Alpert, Validation of filter integrity by measurement of the pore distribution function, Pharmaceut. Technol., February (1992) 32–43.
[21] P. Grabar and S. Nikitine, Pore diameters of colloidon membranes used in ultrafiltration, J. Chim. Phys., 33 (1936) 721–741 (in French).
[22] H. Bechhold, M. Schlesinger and K. Silbereisen, Pore size of Ultrafilters, K. Zeitsch., 55 (1931) 172–198 (in German).
[23] F.A.L. Dullien and V.K. Bartra, Determination of the structure of the porous media, Ind. Eng. Chem., 62(10) (1970) 25–53.
[24] J. Pich, Gas filtration theory, in M.J. Matteson and C. Orr (Eds.), Filtration Principles and Practices, 2nd edn., Marcel Dekker, NY, USA, 1987, pp. 1–132
[25] G. Tkacik and A. Bartlett, Composite microporous membranes, US Pat., 5,228,994 (1993)